75th International Astronautical Congress (IAC), Milan, Italy, 14-18 October 2024.

IAC-24-A6.10-E9.4.1

Extending a Risk Metric for Individual Missions to Evaluate Overall Risk in Orbit

Callum Wilson[1, a)*], Massimiliano Vasile[1], Jinglang Feng[1], Keiran McNally[2], Nina Maric[2], Andre Horstmann[3]

[1] *Department of Mechanical and Aerospace Engineering, University of Strathclyde, 75 Montrose Street, Glasgow G1 1XJ, United Kingdom*
[2] *GMV, Airspeed 2 Eight Street, Harwell, Oxfordshire OX11 0RL, United Kingdom*
[3] *ESA/ESOC - European Space Operations Centre, Robert-Bosch-Str. 5, 64293 Darmstadt, Germany*
[a] *callum.j.wilson@strath.ac.uk*
[*] *Corresponding author*

Abstract

Assessing the risk associated with new missions in orbit has become increasingly important. With the large number of spacecraft and debris now in orbit, there are many more close encounters between objects, which makes it more difficult to estimate the risk over the lifetime of a mission. Several approaches exist for determining the collision risk associated with a single object. This work uses a novel methodology for calculating the induced risk of a mission to define a more general measure of risk in the space environment. Risk is quantified as the product of likelihood and severity. Likelihood refers to the likelihood of a collision occurring and severity refers to the consequence of a collision. The proposed approach approximates collision likelihood between populations of objects based on the intersection of their distributions. This intersection computes the probability of the minimum orbit intersection distance between the distributions being less than a threshold distance value and scales this probability based on the number of objects. The model of severity uses data from simulated fragmentation events to model the likelihood of collisions with fragments based on parameters of the collision. These values of likelihood and severity give a risk measure for an individual object. We extend this metric to the whole environment by summing the risks associated with each object in the environment. The resulting metric considers the distribution of objects not only in altitude but also over orbital parameters of inclination and eccentricity, as well as right ascension in GEO. Example results are shown for baseline environment conditions and a range of future projected scenarios in LEO, MEO, and GEO regimes. The proposed risk metric requires assumptions on the covariance and masses of objects as well as defining the threshold distance for calculating the intersection. We further examine the effect of varying these parameters to see how different modelling assumptions would affect the metric.

Keywords: Space Environment, Collision Risk, Debris Index

1 Introduction

The recent increase in space traffic has seen a renewed interest in modelling risk in the space environment amid growing concerns around the debris environment. Early research in space environment modelling highlighted limits to the capacity of orbital regions [1]. Now we are at a stage where there are more objects in orbit than ever before and we could be approaching these limits [2]. Therefore, it is important to find new ways of assessing the overall health of the space environment and to monitor how this might change in the future.

In response to this need, many metrics have been proposed to quantify the criticality of individual missions and the overall space environment. Most of these are "risk-based" metrics that compute a likelihood and severity to determine the overall risk [3]. Likelihood refers to the probability of collision and severity the consequence of collisions. Due to the large number of objects in orbit, particularly in Low Earth Orbit (LEO), it can be difficult to estimate the probability of collision between all objects. In addition, determining the consequences of collisions requires estimating the effects of all fragments resulting from a collision. This is expensive to simulate and therefore cannot be simulated for every possible collision.

Existing risk-based metrics calculate the likelihood and severity in a variety of ways. The Criticality of Spacecraft Index (CSI) does not explicitly calculate severity but instead has a single formula for overall risk [4]. This considers densities of objects in orbital shells with an additional

term to account for inclination. Each term in this index is also normalised with respect to a reference value. The Environmental Consequences of Orbital Breakups (ECOB) index evaluates the risk of fragmentations from collisions and has also been extended to consider explosions [5, 6]. Collision likelihood in this metric is based on the density of objects in the relevant orbit while excluding larger objects that can be avoided. The severity term is based on the increased collision probability for operational satellites. Both these terms are evaluated over orbital parameters of Semi-Major Axis (SMA) and inclination. The criticality index developed by ISTI/CNR uses debris flux for estimating collision likelihood [7, 8]. The severity depends on the persistence of debris from a fragmentation event and a term related to inclination, since debris at certain inclinations can result in more collisions. As with CSI, values are normalised with respect to reference values. Previous work by JAXA proposed two formulations of a debris index of differing complexity [9]. The simplest formulation is the product of mass, area, and debris flux on an object. Then the more complex formulation considers the expected number of fragments generated by a collision based on extensive simulations using the NEODEEM debris environment simulator [10].

The metric introduced here is based on previous work defining a measure of risk for individual missions [11]. This risk metric was designed to be suitable where there are many background objects and for missions consisting of single satellites, swarms, or large constellations. It is also applicable to objects across the orbital regions of LEO, Medium Earth Orbit (MEO), and Geostationary Earth Orbit (GEO) and can take into account distributions across all orbital elements. As with other risk-based metrics, this can be extended to the overall environment by summing the risk associated with each object. This provides a simple metric for quantifying overall health as well as seeing how different objects affect the metric.

Most measures of risk will have parameters that can be varied depending on different modelling assumptions. For example, there may be different levels of uncertainty associated with object locations. Although it is desirable to report a single value for the environment metric to allow for comparisons, it is worthwhile exploring how different assumptions may affect the predicted health of the environment. To this end, this study investigates the effect of changing some parameters of the risk metric on its output. In addition, we apply the metric to a reference population simulated over 100 years using default parameters which can be compared to other metrics.

The remainder of this paper is organised as follows. Section 2 describes the method for calculating the risk associated with an individual object and the extension to the whole environment. Section 3 introduces the scenarios and different parameter values used to test the risk metric, the results of which are presented in section 4. Section 5 gives conclusions and future work.

2 Methods

This section describes the risk metric for individual missions that is used to determine overall risk. The metric has two components of collision likelihood, l_{col} and severity, sf_{col}. The risk associated with a single object, R_i is calculated as

$$R_i = l_{col} \cdot sf_{col} \tag{1}$$

The total risk metric, R_{env} is the sum of risks for all objects in the environment

$$R_{env} = \sum_{i=1}^{N} R_i \tag{2}$$

where N is the total number of objects in the relevant regime used to calculate the metric. The following sections describe the steps to calculate collision likelihood and severity.

2.1 Distributions of RSOs and Individual Objects

The background population of Resident Space Objects (RSOs) is modelled as a probability distribution across the relevant orbital regime. This allows a quick estimation of collision likelihood without needing to calculate all-vs-all conjunction probabilities. Gaussian Mixture Models (GMMs) are a suitable class of multivariate distributions for modelling the background population, which have a probability density of the form:

$$p(\mathbf{x}) = \sum_{i=1}^{K} w_i \phi(\boldsymbol{\mu}_i, \boldsymbol{\Sigma}_i) \tag{3}$$

where $\mathbf{x}$ is the vector of modelled parameters, K is the number of mixture components, $\phi(\boldsymbol{\mu}_i, \boldsymbol{\Sigma}_i)$ is the density of a multivariate normal distribution, and w_i is the weight of the ith component. In this case the parameters $\boldsymbol{x}$ are Keplerian orbital elements. In LEO and MEO, the RAAN and argument of pericentre are assumed to be uniformly distributed across the RSOs. Therefore, in these

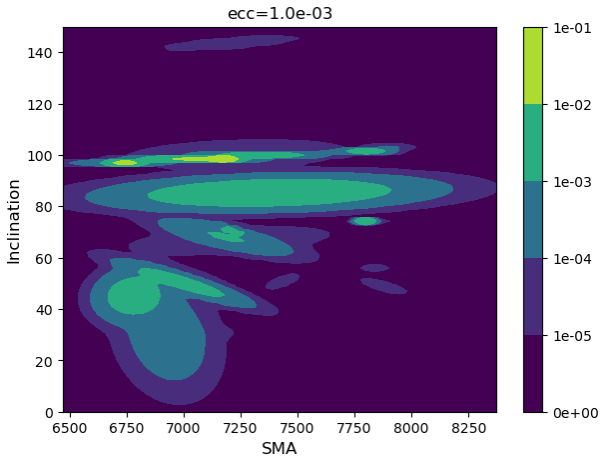

Figure 1: Density of GMM fit to locations of RSOs in LEO for a fixed eccentricity of 0.001.

regimes the only parameters modelled in the GMM are SMA, eccentricity, and inclination. Objects in GEO have a stronger dependence on RAAN and argument of pericentre, so in this regime these parameters are included in the GMM. Fig. 1 shows the density of an example GMM fit to SMA, eccentricity, and inclination of RSOs in LEO, where a higher density value indicates more objects for those orbital parameters.

Individual objects in the environment are considered to have a known orbit with small uncertainties. This means that each object can be modelled as a single peaked multivariate Gaussian with a variance that depends on the accuracy of satellite tracking. As with the model of RSOs, the RAAN and argument of pericentre can be assumed uniformly distributed for a mission, except in GEO or specific orbits such as frozen orbits, where they are included in the distribution.

2.2 Collision Likelihood via Intersection of Distributions

The collision likelihood between an object and RSOs is calculated from the intersection of their distributions. Instead of converting from orbital elements to covariances in cartesian coordinates, the proposed approach uses the Minimum Orbit Intersection Distance (MOID) between the distributions to approximate collision likelihood. For a threshold value ν, the probability that the MOID between the distributions is less than this value can be expressed as

$$p(\text{MOID} < \nu) = \int\int_{\text{MOID}<\nu} (p(\mathbf{x}_{sat})p(\mathbf{x}_{bkgd}))\, d\mathbf{x}_{sat} d\mathbf{x}_{bkgd}, \quad (4)$$

where $\mathbf{x}_{sat}$ and $\mathbf{x}_{bkgd}$ are the orbital parameters of the object of interest and the background population, respectively. The integral is taken over the space of orbital parameters where the MOID is less than the threshold ν. Equation 4 can be numerically approximated via Monte-Carlo integration by sampling points from the distributions of the object of interest and background population and finding the points where the MOID is less than the threshold value. This is calculated as

$$p(\text{MOID} < \nu) = \frac{1}{N_I} \sum_{i=1}^{N_I} (p(\mathbf{x}_{sat}^{(i)})p(\mathbf{x}_{bkgd}^{(i)}) (\text{MOID}^{(i)} < \nu) V_{sat} V_{bkgd}), \quad (5)$$

where N_I is the number of samples used to integrate, $\mathbf{x}_{sat}^{(i)}$ and $\mathbf{x}_{bkgd}^{(i)}$ are orbital parameters sampled from the distributions of the object of interest and background population, respectively, $(\text{MOID}^{(i)} < \nu)$ is 1 when the MOID is less than the threshold and 0 otherwise, and V_{sat} and V_{bkgd} are the volumes of orbital parameters over which the distributions are sampled. In the case of a single object, V_{sat} is the volume of a hyperellipsoid with radius 6σ in each direction, where σ is the variance of the relevant orbital parameter. Samples from the background population are taken from a range of each parameter, so V_{bkgd} is the volume of a hypercuboid with side lengths of the range of each parameter. The calculation of the MOID between two samples of orbital parameters uses a fast implementation to maintain the overall speed of the method [12].

To account for the number of objects in the population, the probability is scaled to give the collision likelihood:

$$l_{col} = N_{sat} \cdot N_{bkgd} \cdot p(\text{MOID} < \nu) \quad (6)$$

where N_{sat} is the number of objects for which the risk is calculated, which is always 1 when considering a single object, and N_{bkgd} is the number of objects in the background population. This value gives an estimate of the likelihood of collision between two populations of objects.

2.3 Severity Factor

The severity of a collision has two parts: the induced severity and the encountered severity [11]. "Induced"

refers to the additional risk of collision in the environment caused by debris from a collision. "Encountered" refers to the effect of a collision on the object of interest. In this risk metric, we are interested in the induced risk, i.e. the effect of a collision on other objects in the environment.

This induced severity factor uses simulations of fragmentation events to calculate their collision likelihood with a distribution of objects and fits a simple model to estimate this probability. The procedure for modelling the severity is as follows:

1. Simulate a number of fragmentations with the NASA Standard Breakup Model (SBM),
2. Propagate each fragment cloud for 10 years,
3. Determine a worst-case payload population based on the current population and 10-year launch model,
4. Find the collision likelihood between this population and each propagated fragment cloud,
5. Fit a function of the collision and environment parameters to estimate the collision likelihood for each fragment cloud – equivalent to the induced severity.

The first step is to run simulations of collisions over a range of orbital and collision parameters. Further details of these simulations can be found in [11]. The output of these simulations are orbital parameters of fragments that are then propagated for 10 years. After this time, the fragment band will have spread across the orbital shell in RAAN and so its distribution does not change significantly.

Future launches are modelled as an exponential-logistic curve of the total number of objects launched per year. This curve has the following form:

$$N(t) = n_0 + \frac{Ae^{d(t-t_0)}}{b + e^{-c(t-t_0)}} \tag{7}$$

where N is the number of objects, t is the year, and the other parameters are adjusted to closely replicate historical launches while giving a reasonable future trend. Using the categories of objects as defined on DISCOSWeb[1], launched objects are either Payloads, Rocket Bodies, or Mission Related Objects (MROs). The proportion of each is taken from historical data and used to calculate the number of launched payloads as a fraction of the total number of objects. The orbital and physical parameters of newly launched payloads are modelled as a GMM fit to historical data and sampled for each launched object. As a worst-case assumption, all currently active payloads and newly launched payloads over ten years are assumed to remain active. Therefore the future payload population is taken as the current payload population plus launched payloads.

With the populations of future objects and propagated fragments defined, the next step is to estimate the likelihood of collision between these two populations. This is done using the same approach as described in Section 2.2 by fitting a GMM of both populations and finding the intersection via Eq. 5. This is used to calculate the likelihood via Eq. 6, where N_{sat} is the number of fragments after 10 years and N_{bkgd} is the number of objects in the estimated future object population. This gives the likelihood of fragments from each simulated event colliding with the future population, which are then used as training data for the severity model.

The final step in defining the severity factor fits a simple model to the simulated probabilities of collision with fragments. The features of a collision used to estimate the severity factor are:

- Equivalent mass M,
- Density of background objects ρ,
- Normalised object decay rate r_{decay}.

The equivalent mass comes from the NASA SBM and is defined as

$$M = \begin{cases} m_{target} + m_{chaser} & \text{if } E > 40J/g, \\ m_{chaser} \cdot \frac{v_{rel}}{1000} & \text{otherwise,} \end{cases} \tag{8}$$

where m_{chaser} is the median mass of all objects at the start of the relevant simulation and v_{rel} is assumed to be twice the circular orbit velocity at the altitude of the object. The density of background objects comes from a kernel density estimate over altitude of the future population as defined above. This value is used since fragmentations in more densely populated altitudes are likely to result in higher collision likelihoods. In GEO, the density of objects in RAAN can also affect the future collision likelihood. To account for this, the density term in this regime is the sum of densities in altitude, ρ_a and RAAN, ρ_r. Fig. 2 shows the variation in ρ over altitude in MEO for an example future population of objects.

The final feature is the decay rate. Some of the fragments in each simulated scenario will decay over the 10-year propagation duration. The proportion of fragments

[1] https://discosweb.esoc.esa.int/

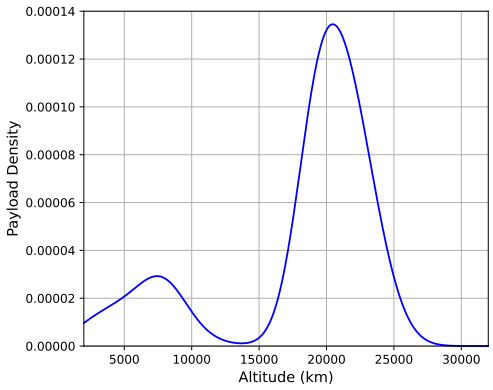

Figure 2: Kernel density estimate over altitude of future payload population in MEO.

that decay depends on the altitude as shown in Fig. 3. This trend can be captured using the log-exponential model of Eq. 7 by replacing the year t with the altitude h in metres. The parameters shown in Fig. 3 are calculated using a least-squares fit.

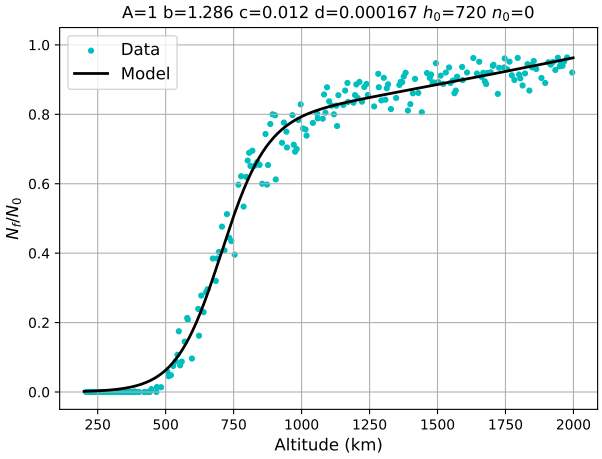

Figure 3: Log-exponential model of decay rate of fragments in LEO.

The severity factor takes the following form:

$$sf_{col} = a \cdot M^{0.75} \cdot \rho^{b} \cdot r_{decay} \tag{9}$$

where a and b are coefficients calculated using a least-squares fit for each regime and the terms M, ρ, and r_{decay} are calculated as described above. After fitting the values of a and b to simulated fragmentations, Eq. 9 can be used to estimate the severity of a fragmentation event without needing to propagate all fragments. Further details on the simulated fragmentations and model fit can be found in [11]. The calculated coefficients for each regime are shown in Table 1.

Table 1: Severity factor coefficients.

Regime	a	b
LEO	2.31e+4	0.229
MEO	1.49e+6	1
GEO	27.14	-0.21

3 Test Scenarios

This section describes the scenarios for applying the risk metric described above. To test the effect of changing the parameters of the model, this metric was applied to a range of scenarios across LEO, MEO, and GEO with different parameters. The process for creating these scenarios is described below. Using a default set of parameters, further tests were carried out using a reference environment simulation, which is also described below.

3.1 Launch Scenarios

In these scenarios, an initial population of objects is propagated with new objects added via launches and fragmentations. The launch model uses the log-exponential curve of Eq. 7 to model the total number of objects launched each year. An alternative to this trend is to assume a linear increase in number of objects launched as follows:

$$N(t) = m \cdot t + c_0 \tag{10}$$

where the parameters m and c_0, are selected to produce the desired trend. Then the orbital and physical parameters are sampled from a GMM fit to historical data. A more detailed description of this launch model can be found in [13].

This study uses three different launch scenarios: no launches, realistic, and worst-case. Table 2 lists the launch model parameters for the realistic and worst-case scenarios. The models for the total number of objects launched for LEO and GEO use Eq. 7 and for MEO Eq. 10. In LEO, this trend excludes constellation payloads, which are added separately based on planned future constellations. Table 3 shows 6 of the largest current and planned constellations, including missions that already have a substantial number of operational payloads. These values are used to estimate the number of additional payload launches each year to maintain the constellation.

Table 2: Launch model parameters for different scenarios in each orbital regime.

Regime	Scenario	A	b	c	d	t_0	n_0	m	c_0
LEO	Realistic	1100	0.8	0.2	0.002	2025	100	-	-
	Worst-case	2000	1.3	0.4	0.03	2024	150	-	-
MEO	Realistic	-	-	-	-	-	-	0.8	5
	Worst-case	-	-	-	-	-	-	1.8	10
GEO	Realistic	-12	1	0.3	0.0001	2030	23	-	-
	Worst-case	50	1.8	0.9	0.008	2025	25	-	-

Table 3: Parameters of some planned constellations.

Name	Number of Spacecraft	Deploy Start	Mission Start	Lifetime (years)	Mass (kg)	SMA (km)	Ecc.	Inc. (°)
OneWeb	648	2020	2023	10	147	7578	1e-4	87.9
Starlink	8064	2020	2023	5	386	6938	1e-4	53
Spire Global	110	2020	2023	2	5	6868	1e-4	51.6
Amazon Kuiper	3264	2024	2025	7	650	6988	1e-4	51.9
Telesat	300	2026	2027	10	700	7626	1e-4	50.88
Boeing	147	2026	2027	10	3000	7463	1e-4	50

Simulations were run using ESA's DELTA software with all force models in the propagator and fragmentations resulting from collisions and explosions. Table 4 shows the change in the number of objects for each scenario at the start, mid-point, and end of the 50-year simulation. LEO shows the most substantial change in numbers of objects across the different scenarios, whereas in GEO there is little change resulting from the different launch models.

Table 4: Total number of objects each year for different scenarios across each orbital regime.

Regime	Scenario	Total N Objects		
		2023	2048	2073
LEO	No Launches	19410	16579	17872
	Realistic	19410	109146	211599
	Worst-case	19410	126393	347841
MEO	No Launches	589	616	669
	Realistic	589	903	4706
	Worst-case	589	933	24518
GEO	No Launches	853	799	854
	Realistic	853	799	853
	Worst-case	853	799	854

3.2 Model Parameters

As described in Section 2, the risk model has parameters that can be adjusted based on different modelling assumptions. The two parameters that are analysed here are the MOID threshold ν and the tracking accuracy of the object of interest. In conjunction analysis, it is common to devise measures of risk based on miss distance, where it is possible to relate these measures to probability of collision [14]. Therefore, the MOID threshold can be chosen based on the maximum desired collision probability for an individual encounter. A description of the process for calculating this threshold can be found in [11]. Common thresholds for "high-risk" conjunctions range from 10^{-6} to 10^{-4} [15]. Here we use three values of ν corresponding to probabilities of 10^{-6}, 10^{-5}, and 10^{-4}, which are: $1.05km$, $3.32km$, and $10.51km$, respectively.

The level of tracking accuracy of an object affects its covariance, which in turn will affect the estimated collision likelihood for each object. Table 5 lists the covariances associated with different levels of tracking accuracy for an object's orbital elements. These values are based on those presented for equinoctial elements in [14], which are assumed to be similar for the Keplerian elements used here.

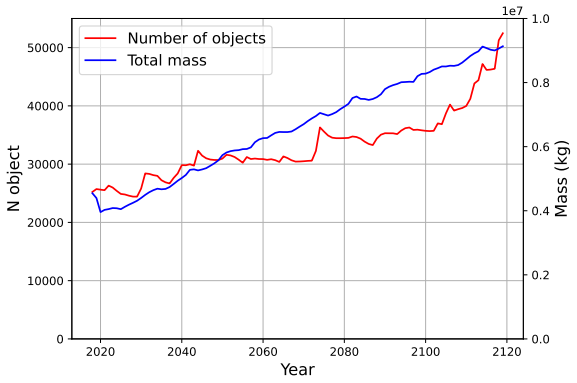

Figure 4: Total number and mass of objects in the reference environment.

Table 5: Variance values for orbital elements with different levels of tracking accuracy.

Tracking Accuracy	SMA (km)	Ecc.	Inc. (°)	RAAN (°)	aPer (°)
Low	20	10^{-4}	10^{-3}	10^{-3}	10^{-3}
Medium	2	10^{-5}	10^{-4}	10^{-4}	10^{-4}
High	0.05	10^{-6}	10^{-5}	10^{-5}	10^{-5}

3.3 IADC Reference Environment

In addition to the scenarios described above, we apply the metric over 100 years to a reference scenario that allows comparisons between different metrics. The scenario shown here is used by the Inter-Agency Space Debris Coordination Committee (IADC) for comparing debris indices[2]. The simulated environment includes repeated launches from historical data and fragmentations. Most of the objects in this scenario are located in LEO; any objects outside of LEO are considered to have a collision likelihood of 0 when calculating the risk metric. Fig. 4 shows the trend in the number of objects and total mass of objects in this scenario, which simulates between the years of 2018 and 2119.

Fig. 5 shows the trend in the number of objects divided into each object type in the reference environment. Across the timescale of the simulation, fragments make up the majority of the number of objects and the number of inactive satellites steadily increases. Fig. 6 shows the trend in the total mass of objects for the same classes of objects. Despite their large numbers, fragments make up relatively little of the overall mass in the environment, which is dominated by upper stages and inactive satellites. As will be shown, this has a substantial effect on the distribution of the risk across objects types.

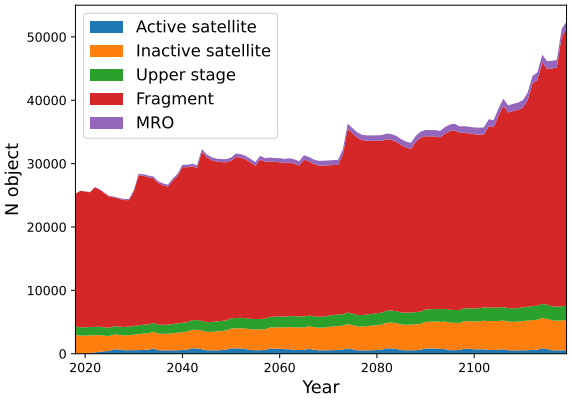

Figure 5: Total number of objects by object type in the reference environment.

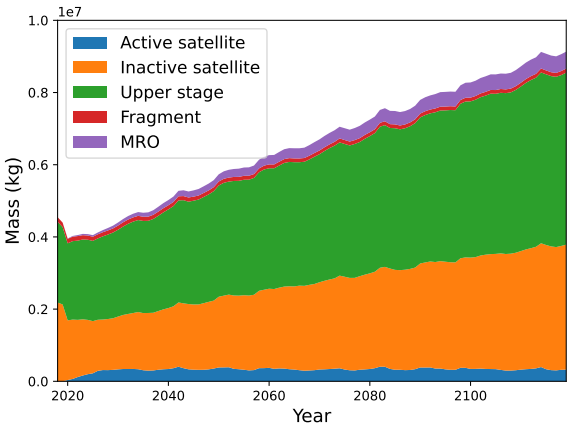

Figure 6: Total mass of objects by object type in the reference environment.

4 Results and Discussion

4.1 LEO

Fig. 7 shows the trend in the metric R_{env} in LEO across the different scenarios and parameters. In the no launches scenario, as expected the total risk remains stable across the simulation duration for each set of parameters. The realistic scenario shows a significant increase in risk for all parameters, noting the log-scale of the plot. The general trend, as observed in most scenarios, is for the metric to decrease with increased tracking accuracy. By defini-

[2]Reference environment developed by Dr Alessandro Rossi for use in IADC debris index studies.

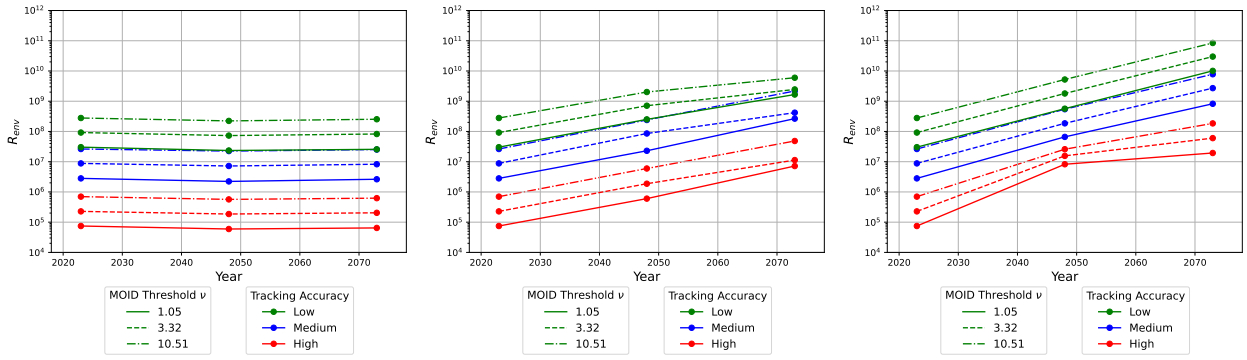

(a) No launches (b) Realistic (c) Worst-case

Figure 7: Risk metric for different parameters and scenarios in LEO.

tion, increasing the MOID threshold results in an increase in the risk as observed across all simulations. In both the no launches and realistic scenario, the risk values for low tracking accuracy and $\nu = 1.05km$ are nearly identical to those of medium tracking accuracy and $\nu = 10.51$. For this range of MOID thresholds, the high tracking accuracy always results in lower risk than the other levels.

Another way of examining the change in trend with different parameters is to look at the normalised value of risk. Here we normalise the risk across each set of parameters with respect to their value in 2023 to observe the relative change in risk. This is shown in Fig. 8 for LEO, since this regime gave the biggest variation in risk across years and scenarios. The no launches case has the lowest variation in normalised risk across runs since in each case the value does not change substantially. While the realistic and worst-case scenarios have a larger range of risk values, the general trend over time is still discernible. This indicates that although the magnitude of the risk metric can change substantially with the model parameters, its relative change over time is more consistent.

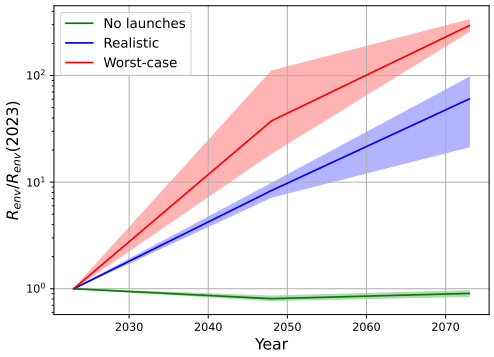

Figure 8: Normalised risk metric across scenarios in LEO. Solid lines indicate mean across all parameters, shaded area indicates minimum and maximum across all parameters.

4.2 MEO

Fig. 9 shows the risk metric trend across parameters and scenarios in MEO. Compared to LEO, the increase in risk in the scenarios with launches are more modest. The worst-case launches also see a slight decrease in risk in the middle of the simulation across parameters. As before, there are also some overlaps in the total risk for different parameter values. What is most interesting to note is that in the no launches case, for the MOID thresholds of $\nu = 1.05km$ and $\nu = 3.32km$, the the total risk is lower with low tracking accuracy than with medium tracking accuracy. This suggests that the collision likelihoods in this scenario experience probability dilution - a phenomenon in encounters where more uncertainty results in lower estimated likelihood [16].

4.3 GEO

The risk metric trend in GEO, shown in Fig. 10, has the strongest dependence on tracking accuracy. The magnitude of the risk metric does not vary substantially across scenarios. However, for the same MOID threshold, the value of the risk metric can vary by as much as 6 orders of magnitude depending on the assumed tracking accuracy. The other notable feature of the trends in GEO is that for low tracking accuracy, different MOID thresholds slightly change the shape of the trend in the no launches and worst-case scenarios.

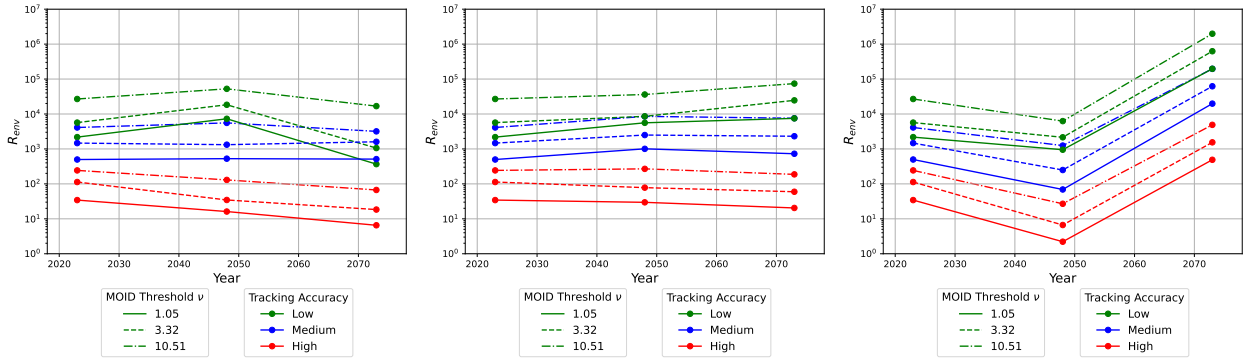

(a) No launches (b) Realistic (c) Worst-case

Figure 9: Risk metric for different parameters and scenarios in MEO.

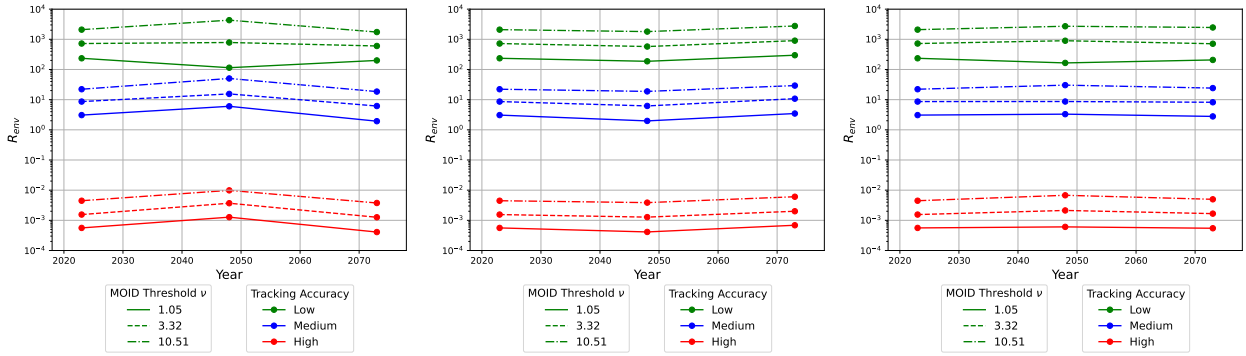

(a) No launches (b) Realistic (c) Worst-case

Figure 10: Risk metric for different parameters and scenarios in GEO.

4.4 IADC

Simulations in the IADC reference environment used a MOID threshold of $\nu = 3.32km$ and variance values for high tracking accuracy (Table 5). Fig. 11 shows the variation in the total risk metric over the 100 years of simulation. While there is some level of noise in the values, there is a clear upward trend which is steeper from around 2100.

Fig. 12 compares the normalised trend of the total risk metric to the number of objects and the square of the number of objects in the environment. Each value is normalised with respect to their value in 2023. Certain trends in the risk match up with those of the number of objects, such as the sharp increase after 2070 and steeper trend after 2100. The square of the number of objects shows better agreement with the trend of the normalised risk metric but the risk metric increases more rapidly. This highlights that the distribution of objects is also significant in determining this metric.

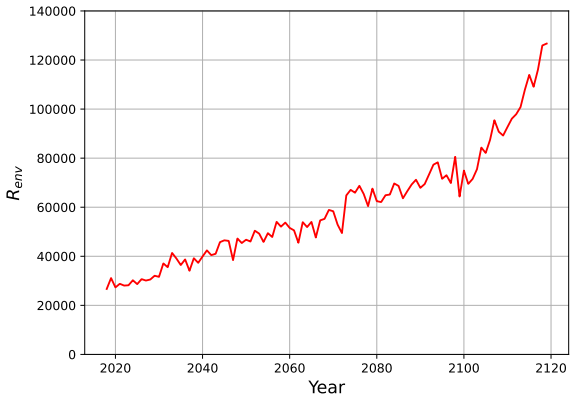

Figure 11: Risk metric trend for the reference environment.

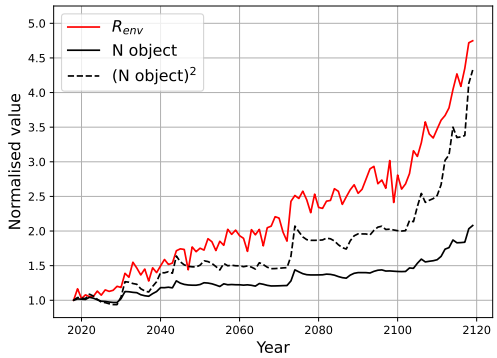

Figure 12: Normalised risk metric for IADC reference environment.

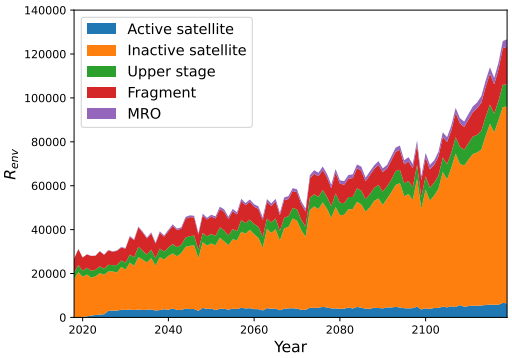

Figure 14: Risk metric by object type for the reference environment.

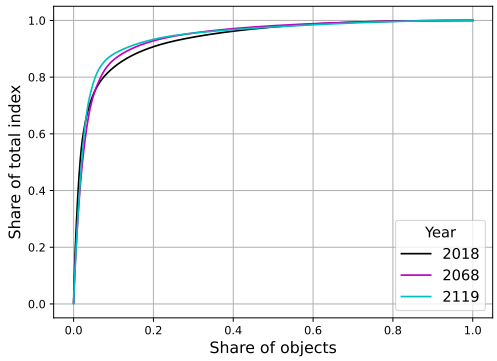

Figure 13: Share of overall risk in the reference environment for individual objects.

In addition to the overall trend, it is possible to identify the contribution of each object and different object classes to the risk metric. Considering the contribution of individual objects, Fig. 13 shows the share of the total risk metric contributed by the share of objects in the environment at the start, middle, and end of the simulation. This shows that the share of contribution does not significantly change over the course of the simulation. Furthermore, in this scenario less than 10% of objects contribute over 80% of the overall risk, which shows the imbalance in risk for each object.

Fig. 14 shows the distribution of risk across each object class in the reference environment. This clearly shows that inactive satellites make up the majority of the risk metric and are most responsible for the steep increase in risk following 2100. This is despite their small share of the overall number of objects as shown in Fig. 5. Although they constitute a significant proportion of the total mass, upper stages make up more of the total mass and far less of the total risk. This is a result of the inactive satellites being located in regions where active payloads are more likely located, giving them a higher severity factor. Note that this risk model does not take into account object manoeuvrability and so the risk is not calculated differently for active or inactive satellites.

As shown in the previous results, the risk model parameters have a strong effect on the magnitude of estimated risk. In LEO, where the risk is evaluated for the IADC reference environment, different tracking accuracies resulted in a change of one order of magnitude in the overall risk and different MOID thresholds saw a change of three orders of magnitude. However, in most cases the trend in the risk over different snapshots remained similar. Although the risk over time in the reference environment is only calculated for one set of parameters, it is reasonable to assume the trend in the risk would be similar for different values of these parameters.

5 Conclusions

This work introduced a new metric for quantifying overall risk in the space environment based on a risk metric for individual missions. The metric is applicable to LEO, MEO, and GEO orbital regions. As with similar risk-based metrics, the proposed metric has parameters that affect the output and two of these parameters have been studied here. The results indicate that the magnitude of the metric can change significantly with the parameters, but the general trend is similar across values of parameters. Results from application to a reference environment also highlight the different relative contribution of object types to the total metric. Since inactive satellites contribute the majority of overall risk in this formulation, this suggests adherence to post mission disposal guidance will be important for improving the long-term health of

the space environment.

Due to the scaling by number of objects, this metric gives a large range of values that can be difficult to compare across scenarios and regimes. Further work is needed to find ways to normalise the metric that allow easier comparisons.

Acknowledgements

This work was partially supported by the European Space Agency under the project "Dynamic Orbital Risk and Safety Assessments in a Changing Space Debris Environment" (Contract Number: AO/1-11137/22/D/KS). The IADC reference environment was developed by Dr Alessandro Rossi for use in IADC debris index studies.

References

[1] D. J. Kessler and B. G. Cour-Palais, "Collision frequency of artificial satellites: The creation of a debris belt," *Journal of Geophysical Research: Space Physics*, vol. 83, no. A6, pp. 2637–2646, 1978.

[2] F. Letizia, B. Bastida Virgili, and S. Lemmens, "Assessment of orbital capacity thresholds through long-term simulations of the debris environment," *Advances in Space Research*, vol. 72, no. 7, pp. 2552–2569, Oct. 2023.

[3] D. McKnight, R. Witner, F. Letizia, S. Lemmens, L. Anselmo, C. Pardini, A. Rossi, C. Kunstadter, S. Kawamoto, V. Aslanov, J.-C. Dolado Perez, V. Ruch, H. Lewis, M. Nicolls, L. Jing, S. Dan, W. Dongfang, A. Baranov, and D. Grishko, "Identifying the 50 statistically-most-concerning derelict objects in LEO," *Acta Astronautica*, vol. 181, pp. 282–291, Apr. 2021.

[4] A. Rossi, G. B. Valsecchi, and E. M. Alessi, "The Criticality of Spacecraft Index," *Advances in Space Research*, vol. 56, no. 3, pp. 449–460, Aug. 2015.

[5] F. Letizia, C. Colombo, H. G. Lewis, and H. Krag, "Assessment of breakup severity on operational satellites," *Advances in Space Research*, vol. 58, no. 7, pp. 1255–1274, Oct. 2016.

[6] ——, "Extending the ECOB space debris index with fragmentation risk estimation," in *7th European Conference on Space Debris*, 2017.

[7] L. Anselmo and C. Pardini, "An Index for Ranking Active Debris Removal Targets in LEO," in *7th European Conference on Space Debris*, 2017.

[8] C. Pardini and L. Anselmo, "Evaluating the environmental criticality of massive objects in LEO for debris mitigation and remediation," *Acta Astronautica*, vol. 145, pp. 51–75, Apr. 2018.

[9] R. Harada, S. Kawamoto, and T. Hanada, "Establishment of debris index evaluation criteria and comparison of index effects," *Acta Astronautica*, vol. 222, pp. 586–595, Sep. 2024.

[10] S. Kawamoto, N. Nagaoka, T. Hanada, and S. Abe, "Evaluation of active debris removal strategy using a debris evolutionary model," in *70th International Astronautical Congress*, vol. 2019-October, Washington D.C., United States, 2019.

[11] C. Wilson, M. Vasile, J. Feng, K. McNally, A. M. Anton, and F. Letizia, "Quantifying the Induced and Encountered Risk of Space Missions," in *74th International Astronautical Congress*, Baku, Azerbaijan, Oct. 2023.

[12] T. Wiźniowski and H. Rickman, "Fast Geometric Method for Calculating Accurate Minimum Orbit Intersection Distances (MOIDs)," *Acta Astronomica*, vol. 63, pp. 293–307, Jun. 2013.

[13] C. Wilson, M. Vasile, J. Feng, K. McNally, A. Antón, and F. Letizia, "Modelling Future Launch Traffic and its Effect on the LEO Operational Environment," in *AIAA SCITECH 2024 Forum*. Orlando, FL: American Institute of Aeronautics and Astronautics, Jan. 2024, p. 1814.

[14] J. T. Horwood, J. M. Aristoff, N. Singh, and A. B. Poore, "A comparative study of new non-linear uncertainty propagation methods for space surveillance," in *Signal and Data Processing of Small Targets 2014*, vol. 9092. SPIE, Jun. 2014, pp. 135–158.

[15] T. Uriot, D. Izzo, L. F. Simões, R. Abay, N. Einecke, S. Rebhan, J. Martinez-Heras, F. Letizia, J. Siminski, and K. Merz, "Spacecraft collision avoidance challenge: Design and results of a machine learning competition," *Astrodynamics*, vol. 6, no. 2, pp. 121–140, Jun. 2022.

[16] S. Alfano and D. Oltrogge, "Probability of Collision: Valuation, variability, visualization, and validity," *Acta Astronautica*, vol. 148, pp. 301–316, Jul. 2018.